

Supporting Information

Atomic-scale study of ambient-pressure redox-induced changes for an oxide-supported sub-monolayer catalyst: VO_X / α -TiO₂(110)

Zhenxing Feng^{1,†}, Lei Cheng^{2,†}, Chang-Yong Kim³, Jeffrey W. Elam⁴, Zhan Zhang⁵, Larry A. Curtiss², Peter Zapol², and Michael J. Bedzyk^{1, 2,6*}

¹Department of Materials Science and Engineering, ⁶Physics and Astronomy, Northwestern University, Evanston, IL 60208, USA

³Canadian Light Source, Saskatoon, SK, S7N 0X4, Canada

²Materials Science Division, ⁴Energy Systems Division, ⁵X-ray Science Division, Argonne National Laboratory, Argonne, Illinois, 60439, USA

*Corresponding author email addresses: bedzyk@northwestern.edu

†These authors contributed equally to this work

I. Primitive unit cell and (110) surface unit cell of α -TiO₂

For convenience of working with the α -TiO₂(110) surface, a non-primitive tetragonal surface unit cell is defined. Figure S1 shows the conventional primitive unit cell (blue dashed lines) with basis vectors \mathbf{a} , \mathbf{b} and \mathbf{c} and the non-primitive surface unit cell (dark black lines) with basis vectors \mathbf{A} , \mathbf{B} and \mathbf{C} , which have lengths $|\mathbf{A}| = |\mathbf{C}| = 6.495 \text{ \AA}$ and $|\mathbf{B}| = 2.959 \text{ \AA}$. The transformation from the primitive tetragonal unit cell to the non-primitive tetragonal unit cell is

$$\begin{pmatrix} \mathbf{A} \\ \mathbf{B} \\ \mathbf{C} \end{pmatrix} = \begin{pmatrix} -1 & 1 & 0 \\ 0 & 0 & 1 \\ 1 & 1 & 0 \end{pmatrix} \begin{pmatrix} \mathbf{a} \\ \mathbf{b} \\ \mathbf{c} \end{pmatrix}$$

Throughout the text of this supplement and the paper, we will refer to the *hkl* values of the primitive unit cell.

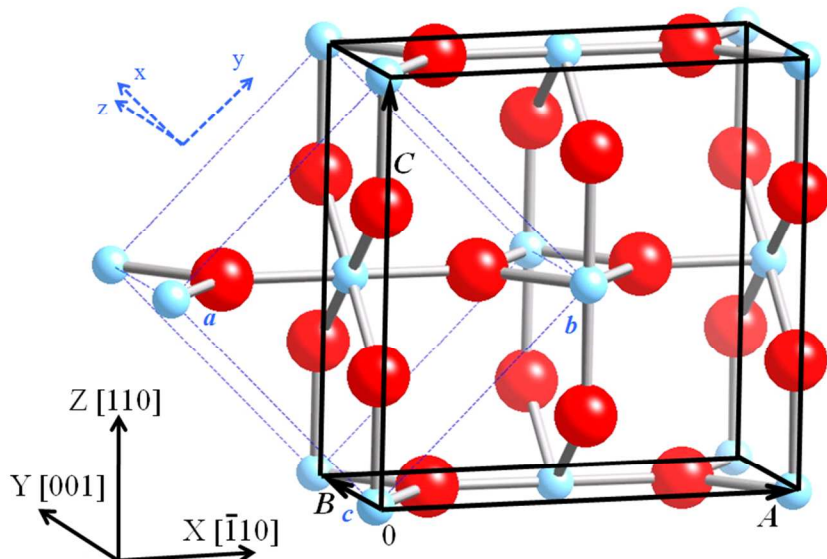


Figure S1. Rutile TiO_2 primitive unit cell (blue dashed lines) and non-primitive (110) surface unit cell (dark black lines). Oxygen atoms are in red and Ti atoms in light blue.

II. Characterization of $\text{VO}_x / \alpha\text{-TiO}_2(110)$ by XPS, AFM and XSW

X-ray photoelectron spectra (XPS) were taken from the blank sample (just after O_2 annealing), and from the as-deposited (AD), oxidized (Ox), reduced (Re) and re-oxidized (Ox2) surfaces. These XP spectra were collected at the Keck II facility of NUANCE at Northwestern University with an Omicron ESCA probe using monochromated Al $K\alpha$ X-rays and a 45° emission angle. A low-energy electron flood gun was used to compensate the XPS induced surface charging effects. Carbon 1s (284.8 eV) was used as the reference to calibrate the XP spectra. Figure S2 shows the survey XP spectra for the blank, AD, Ox and Re $\alpha\text{-TiO}_2(110)$ surfaces. Analyses of these spectra show that the blank surface had 10 at% C. After ALD growth and several days in ambient open-air conditions, the carbon concentration was found to be 22 at%. The oxidized and the reduced surfaces both showed a carbon concentration of 10 at%.. We interpret the 10 at% C in the blank sample to be adventitious carbon resulting from the air transport to the XPS system since the blank TiO_2 sample had been oxygen annealed at 1000°C and this procedure would remove any surface carbon. The 22 at% carbon level measured for the AD sample implies an additional 12 at% C that may result from residual ligands from the VOTP precursor² or from adventitious carbon bound to the V species. The fact that the Ox and Re surfaces showed the lower level of 10 at% C indicates that the Ox and Re treatments removed most of the C contamination from the TiO_2 surface. We expect therefore that the Ox and Re surfaces examined *in situ* by XSW had insignificant C contamination and therefore C should not be seen as affecting the measured surface structures. It of course would be desirable in the future to have access to an integrated preparation-

characterization system that would allow ALD synthesis, XSW measurements, and XPS analysis without air exposure.

Also from analysis of the XP spectra in Figure S2, the V/Ti peak area ratios are found to be 0.29, 0.29 and 0.31 for the AD, Ox, and Re, respectively. Taken together with the less than 1 nm mean-free-path of the emitted electrons, these measurements would indicate that during the redox steps there was no significant loss of V from the surface due to desorption or diffusion.

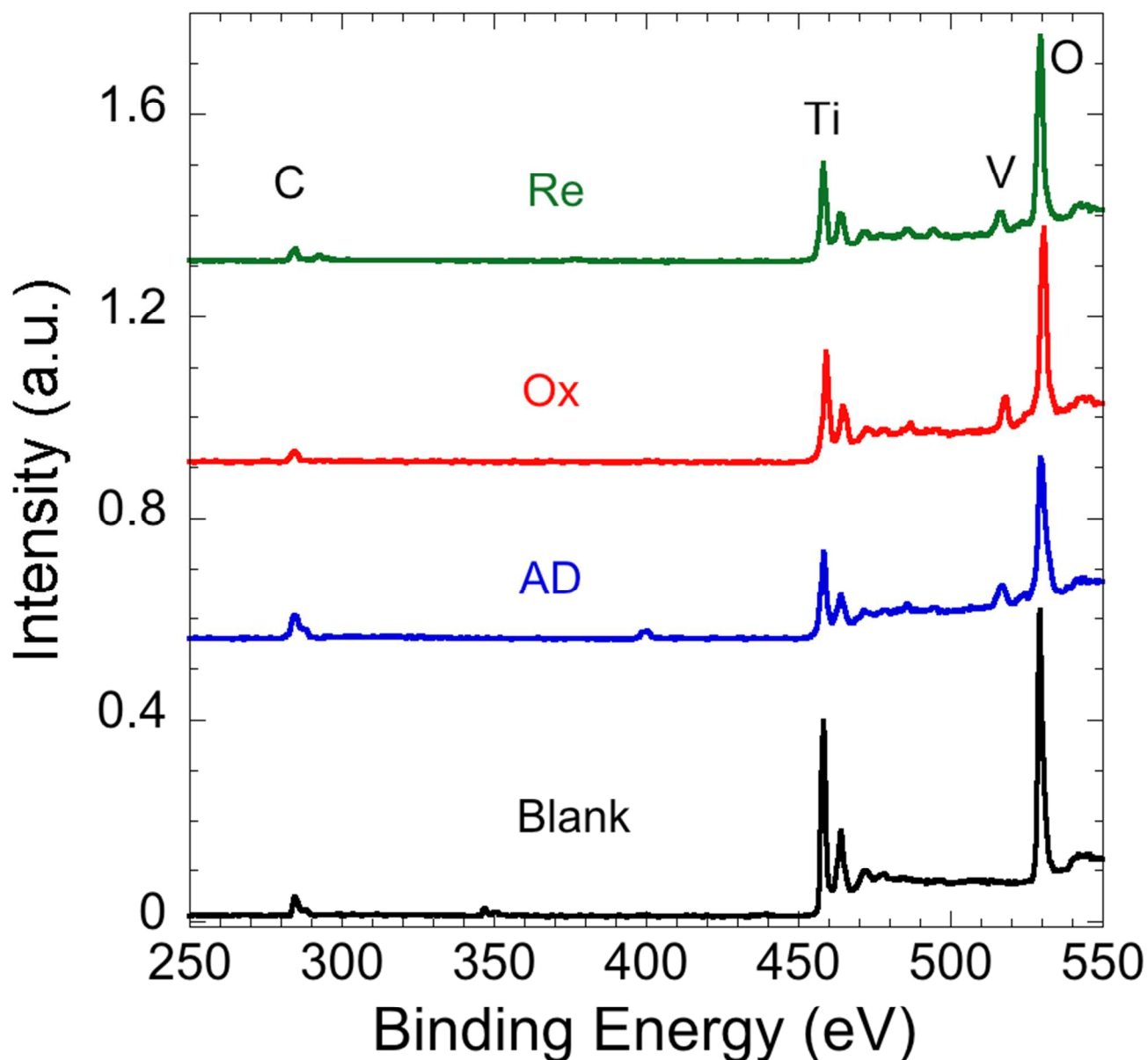


Figure S2. Survey XPS spectra for the blank α -TiO₂(110) surface, and the as-deposited (AD), oxidized (Ox) and reduced (Re) VO_x/ α -TiO₂(110) surfaces. The carbon atomic concentrations are calculated³ to be 10 at% (Blank), 22 at% (AD), 10 at% (Ox) and 10 at% (Re).

To obtain the Ox surface, the sample was placed in a quartz tube furnace. Oxygen was first purged for 10 min. With the continuous oxygen flow, temperature was increased to 180 °C to dehydrate the surface for 10 min and then 350 °C for 30 min to oxidize the surface. After cooling down to room temperature (RT) in oxygen, the sample was immediately transferred into an ultra-high vacuum (UHV) system for XPS and then removed for ambient atomic-force microscopy (AFM) measurements described later. To reduce the surface, the sample was transferred back to the furnace. Followed by a 10 min 5% hydrogen (balanced with nitrogen) purge, the sample was annealed at 350 °C for 30 min. After cooling down to RT in hydrogen condition, the sample was transferred out of the furnace for the same XPS and AFM measurements. The Ox2 surface was prepared with the same steps as used for the Ox surface.

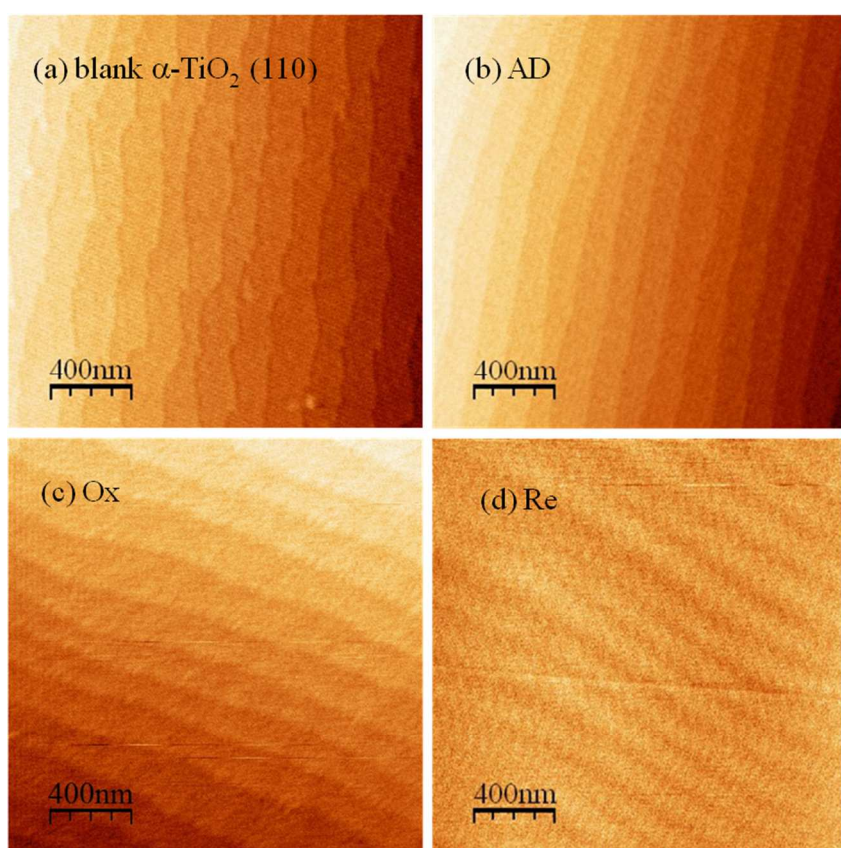


Figure S3. AFM images of the α -TiO₂ (110) substrate surface: (a) after the two-step annealing process AFM shows clean atomically flat terraces with 0.3 nm steps; (b) after ALD deposition (AD), (c) after oxidization (Ox) and (d) reduction (Re).

AFM images were collected in association with each XPS measurement in order to link the chemical state changes with surface morphology changes for the VO_x layer. Silicon AFM tips with a nominal 10 nm radius of curvature and cantilever resonant frequency of 200 kHz was used with a

JOEL-JSPM-5200 scanning probe microscope at the NIFTI facility of NUANCE. The AFM image in Figure S3(a) shows the annealed blank α -TiO₂(110) substrate surface with flat terraces separated by atomic steps. This is the starting point for VO_x ALD. Figure S3(b-d) show that the atomic terraces are preserved after ALD growth and each redox step. Clear terraces at each process indicate that no significant changes have occurred to the rutile surface morphology, i.e., the ALD process is conformal.

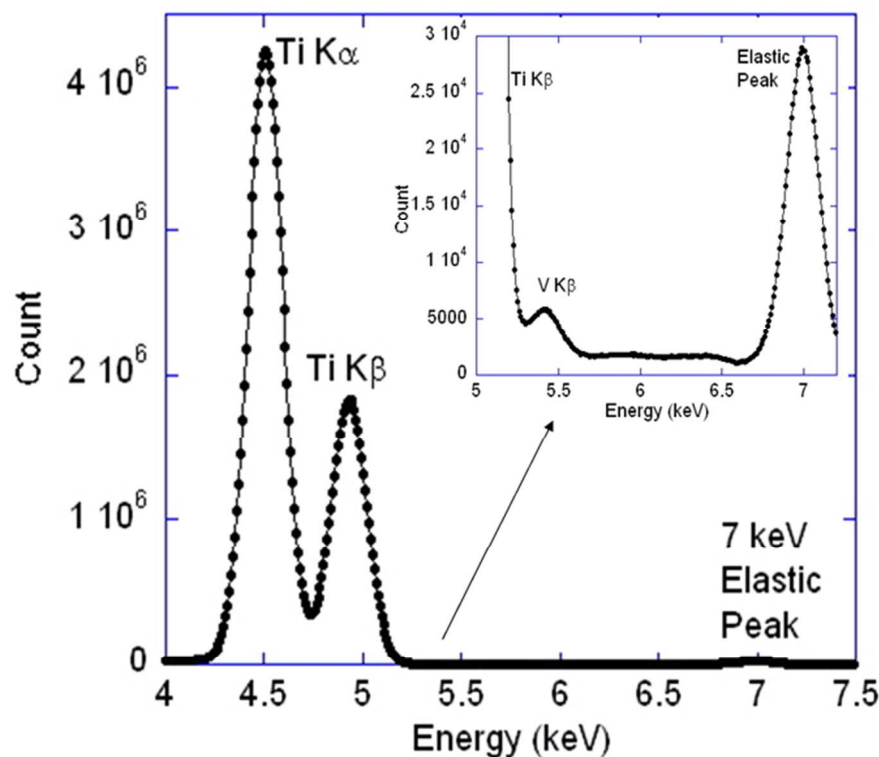


Figure S4. An XRF spectrum of 1.5 ML VO_x/ α -TiO₂ (110) that was collected at an incident photon energy of 7.00 keV and filtered by a 200 μ m thick Al attenuator.

X-ray fluorescence (XRF) and X-ray standing wave (XSW) measurements were performed at the Advanced Photon Source (APS) undulator stations 33ID-D and 5ID-C. An incident photon energy of 7.00 keV was selected with a diamond(111) (at 33ID) and Si(111) (at 5ID) high-heat load monochromator and conditioned further with either Si (111) or (220) channel-cut post-monochromator crystals. A 50 mm² Vortex silicon drift diode (SDD) detector was used to collect the XRF spectra. Figure S4 shows a typical XRF spectrum. In this case, a 1.5 ML VO_x/ α -TiO₂(110) sample was placed on a 4-circle diffractometer. The SDD detector was placed 40 mm away from the center of the sample. Four 50 μ m thick aluminum foils were placed in front of the detector to attenuate the strong Ti K fluorescence signal. The spectrum is dominated by Ti K α (4.51 keV) and K β (4.93 keV) signals. The V K α (4.95 keV) peak is buried under the Ti K β . A small V K β (5.43 keV) peak appears on the tail of the Ti K β peak (Figure S4 inset) and is used for the XSW measurements. For *in situ* XSW measurements,

reduction-oxidation reactions were carried out in a beryllium-dome reaction cell, as described elsewhere⁴. Before oxidation the cell was purged with ultrahigh-purity oxygen (~100 sccm) for 10 min. Then with continuous oxygen flow the temperature was increased to 180 °C for 20 min to dehydrate the sample. This was followed by oxidation at 350 °C for 30 min. The reduction reaction was carried out with a flow (~100 sccm) of 2% hydrogen balanced by 98% helium at 350 °C for 30 min. After the oxidization and reduction reaction steps, the sample was cooled down to 25 °C in the flowing gas, the reaction cell was evacuated by a diaphragm roughing pump, and then XSW measurements were performed at several different hkl substrate Bragg reflections.

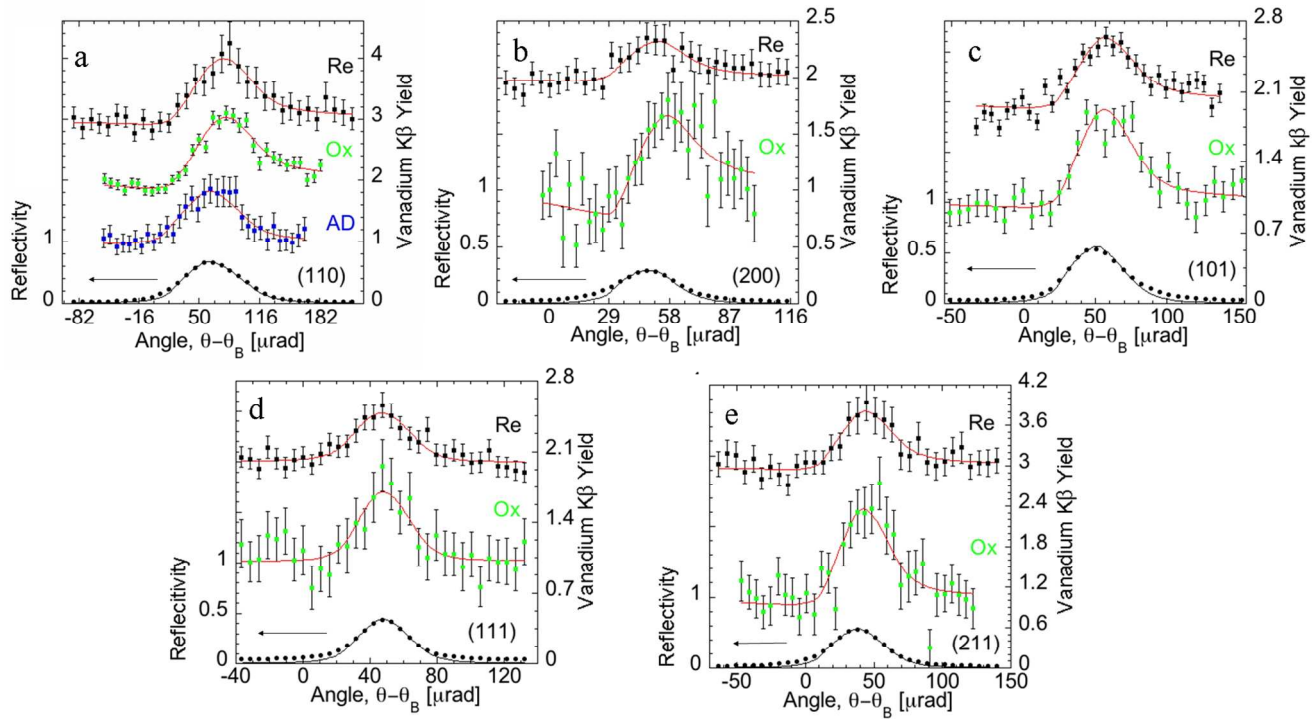


Figure S5. XSW results of (a) (110) normal direction, (b) (200), (c) (101), (d) (111) and (e) (211) off-normal directions of α -TiO₂(110) for as-deposited (AD), oxidized (Ox) and reduced (Re) ALD vanadium oxides. The fluorescence spectra are displaced vertically in the order of processing AD, Ox and Re. The left-side axis is the reflectivity and the right-side axis is normalized vanadium K β yield. Table 1 shows the results of the fit of Eq. S1 to the yield data. For the AD surface $f_{110}=0.18(7)$ and $P_{110}=0.11(8)$.

Figure S5 shows the XSW data and analysis for the (110), (200), (101), (111) and (211) α -TiO₂ Bragg reflections for the AD, Ox and Re states. The XSW induced modulation of the background-subtracted and deadtime-corrected V K β fluorescence yield, $Y(\theta)$, from each scan is used to determine the coherent fraction (f_H) and coherent position (P_H). This determination is based on fitting the normalized yield data for the $H=hkl$ reflection to the model independent expression for the yield^{5,6}

$$Y(\theta) = [1 + R(\theta) + 2\sqrt{R(\theta)} f_H \cos(v(\theta) - 2\pi P_H)] Z(\theta) , \quad (\text{S1})$$

where $R(\theta)$ and $v(\theta)$ are respectively the intensity and phase of the reflected plane wave relative to the incident plane wave. $Z(\theta)$ is the normalized effective thickness. $Z(\theta) = 1$ for surface atoms, such as the V atoms in our case. The shapes of the (110) V fluorescence yields in Figure S5(a) change from symmetrical in the AD condition to more asymmetrical in Ox and Re conditions; indicating that the V atomic distribution relative to the (110) planes changes from uncorrelated to partially correlated. Figure S5(b-d) also show changes in the fluorescence yields from the Ox to Re state, indicating different V atomic distributions for these two cases.

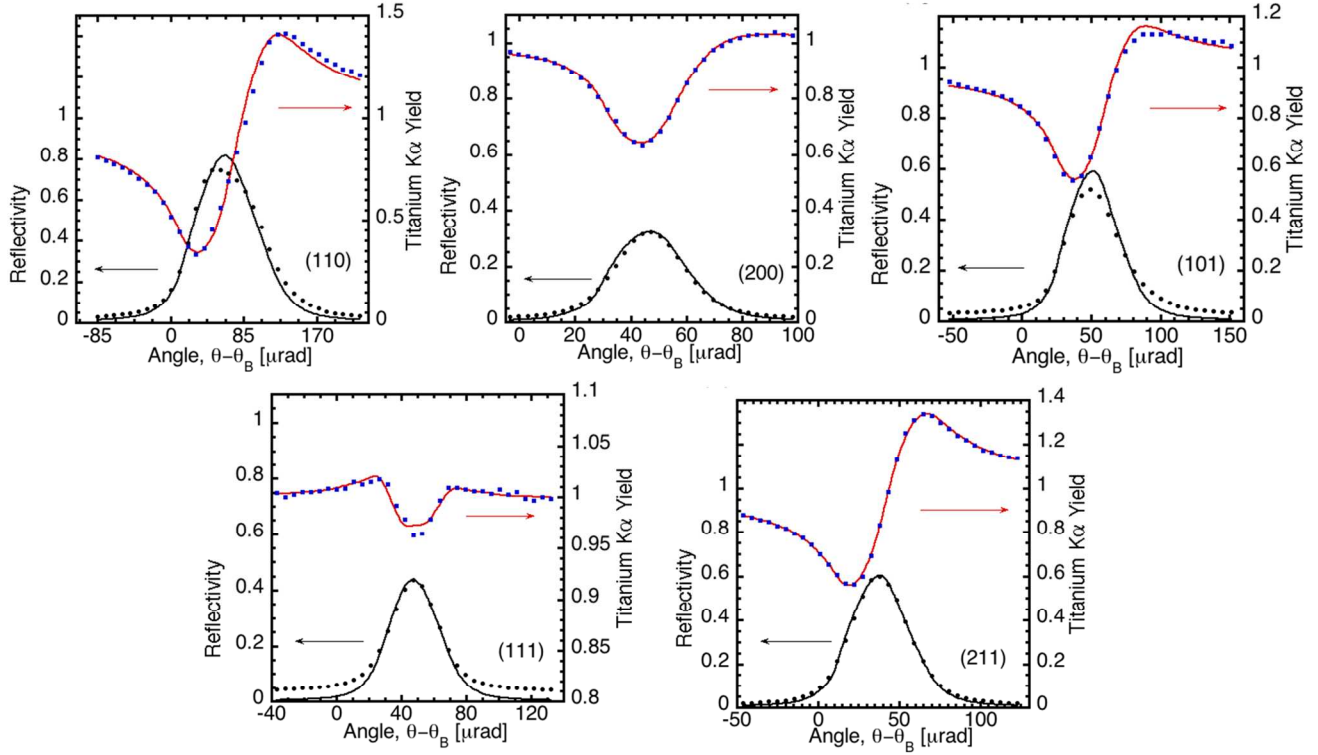


Figure S6. The XSW results for the bulk Ti $K\alpha$ signal for diffraction planes (110) normal direction, (101) , (200) , (111) , and (211) off-normal directions for sample at oxidized state. Table S1 shows the results from the fit of Eq. S1 to this Ti yield data.

To check the validity of our V XSW analysis, the Ti $K\alpha$ signal from bulk α - TiO_2 was also analyzed, as shown in Figure S6. These signals were collected simultaneously with the V signals. The analysis results are listed in Table S1. Note that the XRF takeoff angle, α , refers to the angle between the detector center and the sample surface. It is used for calculating the effective attenuation of the Ti $K\alpha$ fluorescence signal, which includes the extinction effect described by the variable effective thickness $Z(\theta)$ ⁷. Results show that for the (110) , (101) , (200) and (211) planes, the coherent positions are $P_H = 0$ and the coherent fractions are approaching unity as expected. Note that our analyzed value of $f_{111} = 0$ is expected because the (111) reflection is an “oxygen-only” reflection; namely the (111) is a forbidden reflection for the body-centered Ti sublattice. Analysis results are consistent with Ti structure

in bulk α -TiO₂ (110), demonstrating the validity of our XSW analysis for vanadium. By inserting the measured coherent fractions and positions of bulk Ti into Eq. (1), a Ti atomic density map, as shown in Figure S7, is generated with Ti density maxima at the bulk-like Ti sites. This further validates our XSW analysis procedure.

Table S1. XSW analysis of the bulk Ti sublattice of α -TiO₂ (110). The coherent fractions (f) and coherent positions (P) are experimentally determined from the modulations in Ti K α XRF yields shown in Figure S6. The takeoff angles (α) of the detected XRF emission relative to the surface are also listed. The P values are referenced to an origin that coincides with a bulk Ti atom at the AT site. As expected the AT and BR sites are perfectly in-phase with each other for each hkl ; with the exception of the 111 oxygen-only reflection.

hkl	110	101	200	111	211
f	1.00(1)	0.87(1)	0.81(1)	0.06(1)	0.89(1)
P	0.00(1)	0.00(1)	0.00(1)	--	0.00(1)
α (°)	4.2	6.5	49	8	7

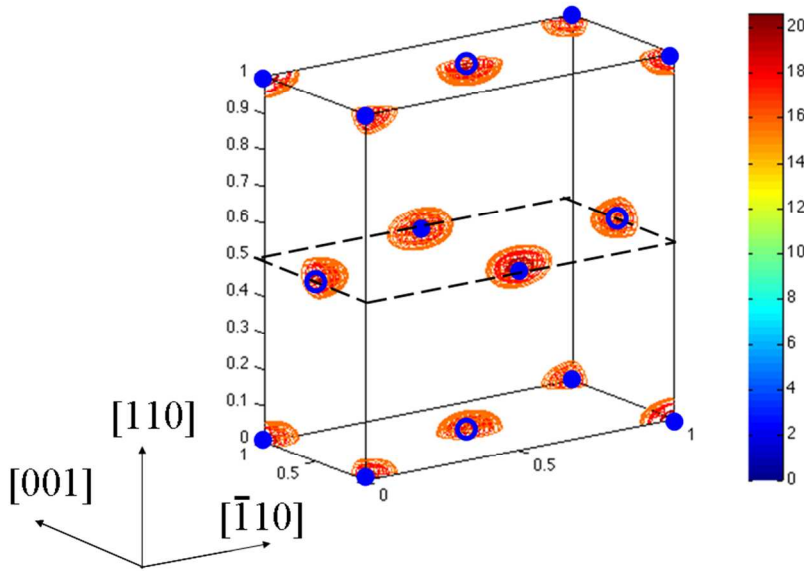


Figure S7. The 3D titanium atomic density map generated by the Eq. 1 summation of XSW measured (hkl) Fourier components listed in Table S1 plus their symmetry equivalents. The Ti atomic density map is superimposed on the same rutile (110) surface unit cell illustrated in Figure 1. As a point of reference open and filled circles denote the two Ti symmetry inequivalent sites in the ideal bulk-like structure with (110) Ti planes at heights of 0, 3.25 and 6.50 Å.

To further analyze the Figure 1 model-independent V maps, several 2D plane-cuts and 1D line-cuts are used. Figure S8 shows the analysis around the AT site at (0,0,0) for V in the Ox state. Numerical analysis of the 3D distribution function around the hot spot gives the center position (0,0,0.054). Three plane cuts ($x=0$; $y=0$; $z=0.054$) and 3 line cuts ($x=y=0$; $x=0$, $z=0.054$; $y=0$, $z=0.054$) are used to examine the properties of the hot spot. A tetragonal box is chosen so that the V atomic

density inside the box is greater than 1. The volume normalized atomic intensity sum in this box gives the occupation fraction of V at this site. Similar analyses are carried out for BR site in the Ox state and the two sites in the Re state. The properties of the hot spots at each site are summarized in Table S2. It clearly shows that the BR to AT occupation ratio, $I_{\text{norm}}(\text{BR}) / I_{\text{norm}}(\text{AT})$, is 4:3 for the Ox state, but 1:1 for the Re state.

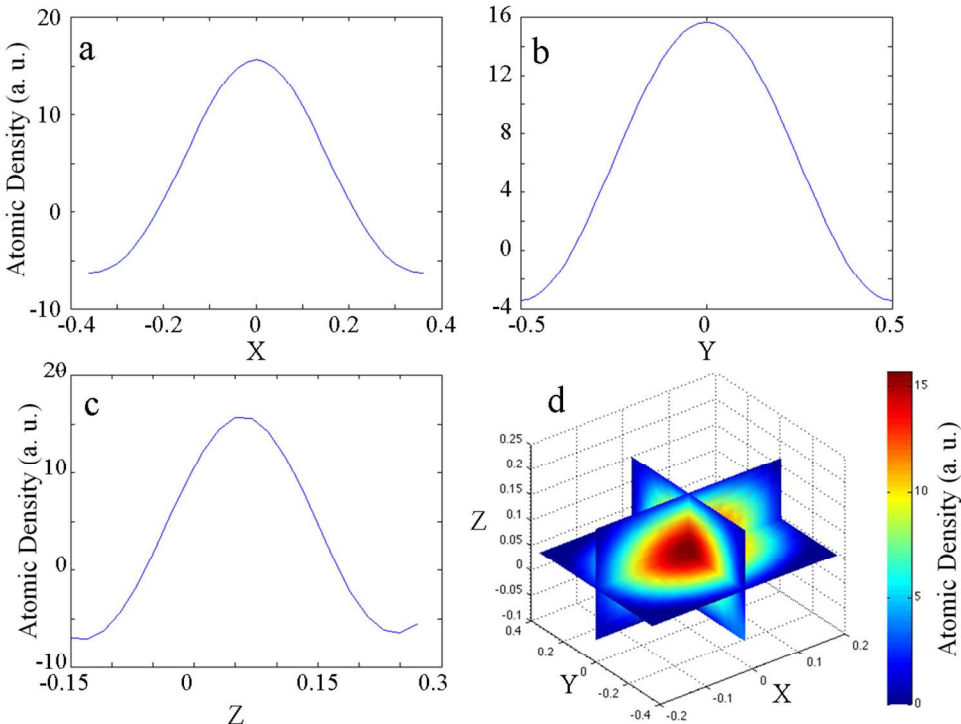


Figure S8. Vanadium model-independent analysis around an AT site: (a-c) 1D line cuts through 3D atomic density map in (a) YZ plane at $Y=0, Z=0.054$; (b) XZ plane at $X=0, Z=0.054$; (c) XY plane at $X=Z=0$; (d) orthogonal 2D plane-cuts through density map around AT site for planes of $X=0, Y=0$ and $Z=0.054$.

Table S2. Numerical analysis of model-independent V atomic distribution $\rho(X,Y,Z)$ around AT and BR sites for the Ox and Re states. The X, Y and Z ranges refer to the range of the tetragonal box chosen for the atomic density integration. The FWHM_i refers to the full width at half maximum in i ($i=X, Y$ or Z) direction. I_{norm} is the volume normalized atomic density sum in this tetragonal box.

	X-range	Y-range	Z-range	FWHM_x (Å)	FWHM_y (Å)	FWHM_z (Å)	Center	I_{norm} (a.u.)
Ox								
AT	[-0.2, 0.2]	[-0.35, 0.35]	[-0.06, 0.18]	1.76	1.33	0.98	0, 0, 0.054	462723
BR	[0.3, 0.7]	[0.19, 0.81]	[-0.04, 0.18]	1.89	1.24	0.98	0.5, 0.5, 0.068	604989
Re								
AT	[-0.25, 0.25]	[-0.25, 0.25]	[-0.17, 0.25]	2.15	1.18	1.04	0, 0, 0.047	337142
BR	[0.25, 0.75]	[0.25, 0.75]	[-0.17, 0.25]	2.15	1.18	1.04	0.5, 0.5, 0.047	337142

III. DFT Calculations of Vanadia Submonolayer on Rutile

In our DFT calculations, the vanadium to oxygen atom ratios in the submonolayer structures were set up to be as close to 2:5 as possible since the XPS measurement has suggested a fully oxidized vanadia submonolayer with +5 vanadium charge and the rutile support is not reduced at the experimental conditions. We also investigated structures with various vanadia submonolayer distributions, surface coverages as well as alignments relative to the rutile (110) lattice, and compared the stabilities of the ones that have stoichiometric vanadium oxide using relative energies defined by:

$$\Delta E = \frac{E_{TiO_2+V_{2n}O_{5n}} - E_{TiO_2}}{n} - \Delta E_0, \quad (S2)$$

where $E_{TiO_2+V_{2n}O_{5n}}$ and E_{TiO_2} are energies of the rutile (110) with vanadia submonolayer and the rutile (110) surface slab, respectively, n is the number of V_2O_5 units in the structure and ΔE_0 is the energy per V_2O_5 unit for the most stable submonolayer structure (Figure S9(a)). For stoichiometric vanadia submonolayer structures, we evaluated stability using Equation S2 and found four most stable structures shown in Figure S9 along with the corresponding relative energies. For the non-stoichiometric vanadia submonolayer structures that we have calculated (not shown except Figure 3(a)), a comparison of the relative stabilities requires knowledge of the vanadium chemical potential due to different ratios of vanadium to oxygen atoms in the submonolayer structure. Thus, we do not report energy for the non-stoichiometric structure shown in Figure 3(a).

The calculated coherent fractions (f) and coherent positions (P) of the two models in Figure 3 are reported in Table 1 of the main text. In addition, the coherent fractions and positions of the structures shown in Figure S9 were also calculated and are reported in Table S3. For the first three low-index directions, for which the experimental measurements are most reliable, the calculated P and f using DFT optimized structures in Figure 3 are in good agreement with the best-fit model and experimental measurements. The coherent parameters of other calculated structures shown in Figure S9 have less agreement with experimental data than those of the two structures in Figure 3.

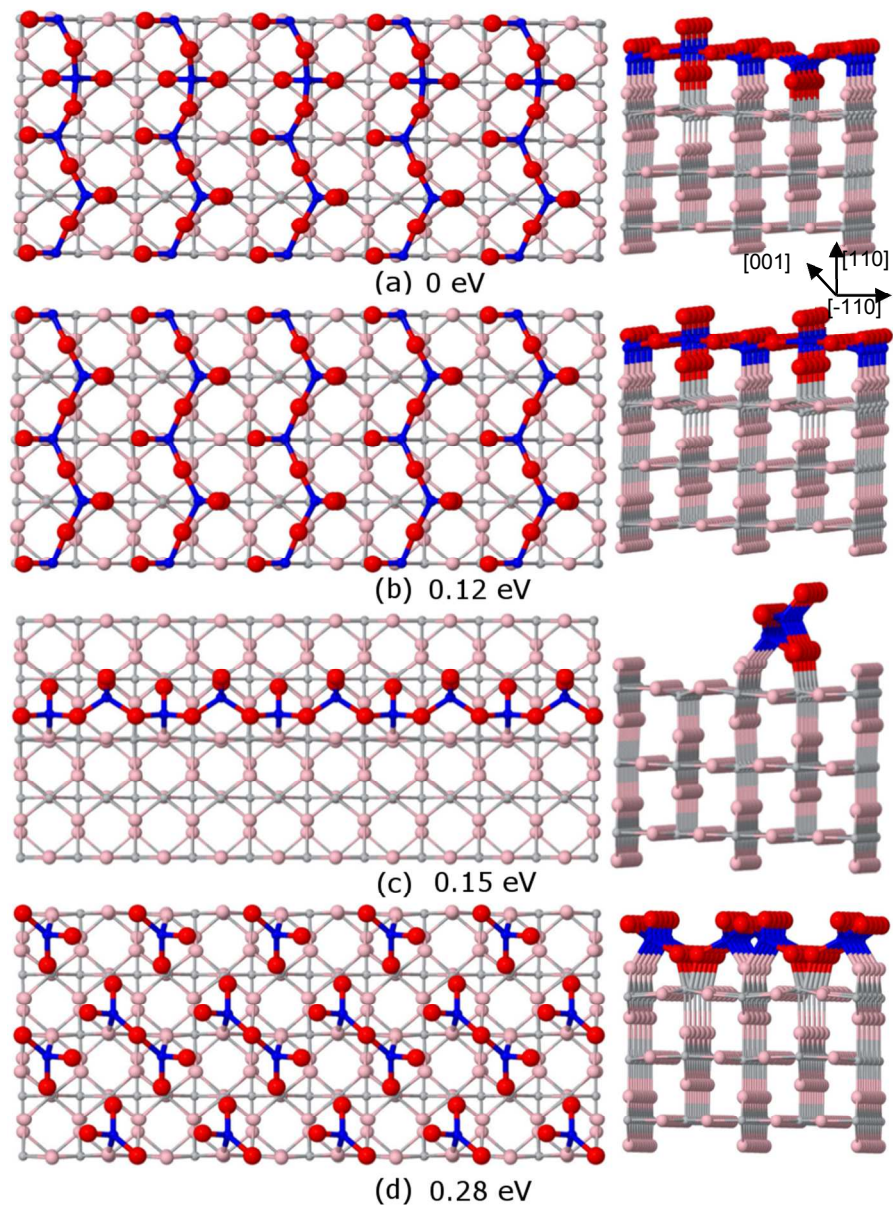


Figure S9. The most stable stoichiometric vanadia submonolayer structures along with their corresponding energies calculated using Equation S2. Titanium atoms are shown in silver and vanadium atoms are shown in blue. Oxygen atoms of the rutile support and V_2O_5 are shown in pink and red, respectively.

Table S3. Coherent fractions (f) and coherent positions (P) of $VO_x / \alpha\text{-TiO}_2(110)$ measured by XSW (P_{meas} and f_{meas}) and calculated from atomic positions in DFT models (P_{DFT} and f_{DFT}) shown in Figure S9. P^1_{DFT} and f^1_{DFT} , P^2_{DFT} and f^2_{DFT} , P^3_{DFT} and f^3_{DFT} , P^4_{DFT} and f^4_{DFT} were calculated using structures in Figure S9 a, b, c and d, respectively.

hkl	P_{meas}	P^1_{DFT}	P^2_{DFT}	P^3_{DFT}	P^4_{DFT}	f_{meas}	f^1_{DFT}	f^2_{DFT}	f^3_{DFT}	f^4_{DFT}
110	0.07(1)	0.03	0.07	0.00	-0.07	0.45(3)	0.31	0.31	0.27	0.34
101	0.16(3)	0.02	0.11	-0.44	-0.05	0.43(7)	0.18	0.06	0.09	0.08
200	0.09(3)	-0.09	-0.22	0.00	-0.08	0.8(1)	0.08	0.05	0.27	0.15
111	-0.26(7)	---	-0.16	-0.30	-0.07	0.3(2)	0.04	0.12	0.08	0.16
211	0.19(3)	0.04	0.28	-0.35	-0.17	0.7(2)	0.15	0.07	0.10	0.08

Reference:

- (1) Elam, J. W.; Groner, M. D.; George, S. M. *Review of Scientific Instruments* **2002**, *73*, 2981.
- (2) Musschoot, J.; Deduytsche, D.; Poelman, H.; Haemers, J.; Van Meirhaeghe, R. L.; Van den Berghe, S.; Detavernier, C. *J Electrochem Soc* **2009**, *156*, P122.
- (3) O'connor, D. J.; Sexton, B. A.; Smart, R. S. C. *Surface Analysis Method in Materials Science*; Springer-Verlag: Heidelberg, 1992.
- (4) Feng, Z.; Kim, C.-Y.; Elam, J. W.; Ma, Q.; Zhang, Z.; Bedzyk, M. *Journal of the American Chemical Society* **2009**, *131*, 18200.
- (5) Bedzyk, M. J.; Cheng, L. *Reviews in Mineralogy and Geochemistry* **2002**, *49*, 221.
- (6) Zegenhagen, J. *Surface Science Reports* **1993**, *18*, 199.
- (7) Bedzyk, M.; Materlik, G. *Surface Science* **1985**, *152*, 10.
- (8) Perdew, J. P.; Chevary, J. A.; Vosko, S. H.; Jackson, K. A.; Pederson, M. R.; Singh, D. J.; Fiolhais, C. *Physical Review B* **1992**, *46*, 6671.
- (9) Kresse, G.; Hafner, J. *Physical Review B* **1993**, *47*, 558.
- (10) Kresse, G.; Hafner, J. *Physical Review B* **1994**, *49*, 14251.
- (11) Blochl, P. E. *Physical Review B* **1994**, *50*, 17953.
- (12) Kresse, G.; Joubert, D. *Physical Review B* **1999**, *59*, 1758.
- (13) Monkhorst, H. J.; Pack, J. D. *Physical Review B* **1976**, *13*, 5188.